ADVANCED ENGINEERING MATERIALS
www.aem-journal.com

Surface Modification of Additively Manufactured Inconel 718 Alloy by Low-Energy High-Current Electron Beam Irradiation

Muhammet Demirtas, Konstantin V. Ivanov, Gencaga Purcek, Harun Yanar, and Yusuf Kaynak*

The effect of low-energy high-current electron beam (LEHCEB) irradiation on the microstructure and nanohardness of Inconel 718 alloy produced by laser powder bed fusion additive manufacturing is investigated. The LEHCEB irradiation is applied to the alloy at three energy levels, and the resulting microstructural analysis of irradiated surfaces is conducted. The findings from this study demonstrate that the LEHCEB irradiation substantially changes the as-built microstructure showing intragranular dendrites of different shapes and irregular-shaped Laves phases. The columnar structure is formed in the modified near-surface layer as a result of rapid heating and cooling during LEHCEB irradiation. Furthermore, all Laves phases dissolve in the modified layer. Nanoindentation hardness of the irradiated layer of the alloy increases from 593 ± 23 to 693 ± 13 H_v with the highest energy density of 15 J cm^{-2}. This increment is attributed mainly to the dissolution of Laves phases and the formation of an ultrafine columnar structure where the columns are separated from each other by the district regions containing very thin interlayers of a secondary phase and a high amount of dislocations.

1. Introduction

Nickel-based superalloys have been widely used for extreme environment applications due to their excellent combination of mechanical properties, corrosion, and oxidation resistance at high temperatures up to 650 °C.[1,2] Among them, Inconel 718 alloy is one of the most commonly used nickel-based superalloys for the parts of aircraft turbine engines, high-speed airframe parts, high-temperature bolts and fasteners applied in nuclear power plants, gas turbines, marine, and aerospace industry.[3,4] Most of the Inconel 718 alloy parts are fabricated using conventional manufacturing technologies like casting and forging. However, it is difficult to produce complex-shaped parts from Inconel 718 alloy using these manufacturing methods since it has low plasticity due to its inherently high strain hardening rate.[5,6] Furthermore, large amounts of material are wasted in conventional manufacturing technologies.[7]

In contrast to conventional manufacturing technologies, additive manufacturing (AM) is a layer-by-layer manufacturing process and it refers to a group of advanced technologies used for fabricating complex functional or end-usable parts through computer-aided design modeling. AM processes offer a wide range of advantages over conventional manufacturing techniques. First of all, it has fewer geometrical constraints and enables the production of complex-shaped parts that cannot be manufactured using conventional manufacturing processes. Such design flexibility provides a significant reduction in the number of parts by eliminating or reducing the need to assemble multiple components, and thus, drastic weight reduction can be achieved by AM. Near-net shaping is another important feature of AM technology, which significantly minimizes material use and waste generation during fabrication. Moreover, AM technology increases the speed of part delivery from conception to market.[8,9] Because of these advantages, AM processes are widely used in various fields. Particularly, the automotive and aerospace industries are the sectors where AM processes have found large applications. This is simply due to light weighting of the component is very crucial in these sectors, and AM processes have enormous lightweighting potential. Although the AM process has many advantages over conventional manufacturing processes, the use of parts manufactured via this method has so far been limited since the as-built parts could have poor surface quality.[10–12] Furthermore,

---

M. Demirtas
Department of Aerospace Engineering
Samsun University
55420 Samsun, Türkiye
E-mail: muhammet.demirtas@samsun.edu.tr

K. V. Ivanov
Institute of Strength Physics and Materials Science
Siberian Branch of Russian Academy of Sciences
Akademichesky 2/4, 634055 Tomsk, Russia

G. Purcek, H. Yanar
Department of Mechanical Engineering
Karadeniz Technical University
61080 Trabzon, Türkiye

Y. Kaynak
Department of Mechanical Engineering, Technology Faculty
Marmara University
34854 Istanbul, Türkiye

The ORCID identification number(s) for the author(s) of this article can be found under https://doi.org/10.1002/adem.202400633.

DOI: 10.1002/adem.202400633

corrosion, wear, and fatigue damages are the most commonly seen failure modes in metallic materials used in engineering components. Accordingly, surface properties have a direct effect on the performance and service life of all components produced by AM, and improved surface conditions can prolong their service life.

In recent years, many studies have been performed to improve the surface quality and mechanical properties of the parts produced by AM to spread the applications of the AM processes. In particular, heat treatment has been preferred to improve the surface and mechanical properties of both wrought and additively manufactured Inconel 718 alloy.[1–4,9,13–16] The main objectives of the postheat treatments can be classified as modifying phase composition and generation of hardening precipitates,[17–21] controlling dislocation cells generated during the build process,[22–24] and controlling grain size.[4,14] The most widely used heat treatments include solutionizing followed by a precipitation hardening step since the primary strengthening mechanism of Inconel 718 is precipitation hardening. In the first step, some undesirable phases, including Laves phase known to decrease mechanical properties, are dissolved in the matrix, and in the second step, the formation of hardening precipitates (γ' and γ'') takes place to harden the material. Hot isostatic pressing[25–27] is another posttreatment method utilized to improve the properties of Inconel 718 alloy produced by AM, and it was shown that it is beneficial to reduce the porosity level of these parts.[28,29] Barrel finishing, shot peening, ultrasonic shot peening, and ultrasonic impact treatment were also applied to Inconel 718 alloy produced by AM to improve the surface properties.[30] It was reported that microhardness was increased while residual porosity was decreased after all of these posttreatment processes.[30] The effects of sandblasting on the fatigue properties of Inconel 718 alloy produced by AM were investigated by Yu et al.[31] It was shown that fatigue resistance of the alloy was significantly improved as a result of the elimination of defects and imposing high compressive residual stress.[31]

Besides these postprocessing techniques, there are limited studies on the surface modification of Inconel 718 alloy produced by laser powder bed fusion (L-PBF) AM using laser shot peening where the concentrated energy source is used.[32] However, the treatments with pulsed electron beams with a pulse duration varying from several microseconds to several hundreds of microseconds[33–35] as another surface modification process with concentrated energy fluxes have not been considered for Inconel 718 alloy produced by L-PBF AM. Pulsed electron beams reveal some advantages with respect to pulsed laser beams including high absorption of incident energy which depends no on the optical properties of the material, and sufficient beam cross-section area up to 100 cm^2.

For example, low-energy high-current electron beam (LEHCEB)[35,36] is characterized by high surface energy density (1–20 J cm^{-2}), short pulse duration (2–4 μs), and moderate accelerating voltage (15–30 kV). Such parameters of the beam enable energy release in a thin near-surface layer resulting in its fast (up to $10^9\ \text{K s}^{-1}$) heating, melting, and partial evaporation if the surface energy density is sufficient. When the pulse ends, the layer quickly ($\approx 10^9\ \text{K s}^{-1}$) cools due to heat transfer to deeper layers.[37] The ultrafast heating and subsequent rapid cooling cause some radical structural changes and phase transformations. These structural alterations mostly bring about an increase in the hardness and wear resistance of the modified surface layer[38–47] in commercially pure metals,[38,39] steels,[40,41] aluminum and its alloys,[42] titanium and its alloys,[43,44] and copper and its alloys.[45–47]

As was noted above, the rough surface and presence of pores reduce the fatigue strength of materials obtained by AM. One of the effects of LEHCEB treatment is porosity elimination in the modified near-surface layer and smoothing of the surface.[48,49] Therefore, LEHCEB treatment can be effective to increase fatigue resistance of additive manufactured materials.

The mentioned studies show that the LEHCEB irradiation can be a promising candidate to modify the surface layer and improve the surface properties of Inconel 718 alloy produced by L-PBF AM.

In the view above, the main purpose of the present study is to investigate the effect of the LEHCEB irradiation on the microstructure and nanohardness of Inconel 718 alloy produced by L-PBF AM. For this purpose, Inconel 718 alloy produced by L-PBF AM was processed via LEHCEB irradiation in a wide range of surface energy densities (E_s). Deep microstructural characterization was performed to investigate the effect of LEHCEB irradiation process on the microstructural alteration of the modified near-surface layer. Furthermore, nanoindentation tests were used to determine the change in surface hardness of the alloy after the irradiation process.

2. Experimental Section

2.1. Materials and Processes

Commercially available Renishaw standard gas atomized Inconel 718 powder with a particle size of 15–45 μm was used for AM in the present study. The nominal chemical composition of the powder according to the data sheet of the powder is given in **Table 1**. The samples with dimensions of $10 \times 25 \times 92\ \text{mm}^3$ were produced by L-PBF AM by using Renishaw AM250 machine in Ar atmosphere. Laser power, scanning speed, layer thickness, and hatch spacing were chosen to be 190 W, 700 mm s^{-1}, 20 μm, and 70 μm, respectively, in the L-PBF process.

The samples having dimensions of $25 \times 20 \times 10\ \text{mm}^3$ were cut from Inconel 718 billets produced by L-PBF AM, as shown schematically in **Figure 1**, using wire-electro discharge

Table 1. Chemical composition of Inconel 718 powder.

Element	Composition [wt%]	Element	Composition [wt%]
Ni	50.0–55.0	Cu	≤0.30
Cr	17.0–20.0	C	≤0.08
Nb + Ta	4.75–5.50	Si	≤0.35
Mo	2.80–3.30	Mn	≤0.35
Ti	0.65–1.15	P	≤0.01
Al	0.20–0.80	S	≤0.01
Co	0–1.00	B	≤0.006
Fe	Bal.	–	–

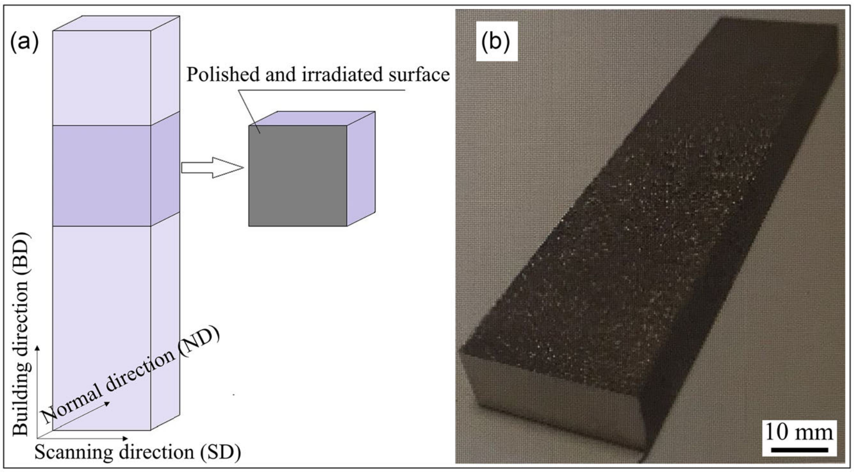

Figure 1. a) Schematic representation and b) real image of the additively manufactured Inconel 718 alloy sample.

machining. The surface of the samples in the building direction-scanning direction (BD-SD) plane before the LEHCEB irradiation was polished to attain a mirror-like surface with an average arithmetical surface roughness of $0.19 \pm 0.03\,\mu m$. To do so, the surfaces were ground first using 150, 1200, and 2500 grit SiC papers, and then polished with 1 μm diamond suspension. During the grounding and polishing processes, the load was kept lower than 5 N to avoid imparting residual stress to the surfaces of the sample.

The LEHCEB irradiation was applied to the Inconel 718 alloy using a RITM-IZ installation equipped with plasma-anode electron gun,[36] as illustrated in **Figure 2**. Processing parameters were as follows: the argon pressure was 6.4×10^{-2} Pa, the pulse number was 10, the accelerating voltage was 27 kV, and E_s were 5, 10, and 15 J cm^{-2}. A heavy ferromagnetic steel cylinder (magnetic field concentrator) placed behind the target was used to focus an electron beam in the latter case.[50] The typical pulse duration measured using an oscillograph was 3.2 μs.

2.2. Microstructural Investigation and Nanohardness Tests

After LEHCEB irradiation process, the surface (BD-SD plane) and cross-section (scanning direction-normal direction (SD-ND) plane) (Figure 1a) were studied using scanning electron microscopy (SEM) in a Carl Zeiss EVO 50 and Apreo 2 (FEGSEM) microscopes. The microstructure of the near-surface and deep layers representing the modified and as-built materials, respectively, was investigated in the cross-section using transmission electron microscopy (TEM) in a JEM 2100 (Jeol) microscope at 200 kV. The phase composition was obtained using selected area electron diffraction (SAED) patterns analysis and energy-dispersive X-ray (EDX) analysis. TEM foils were prepared in SD-ND plane by ion milling in an EM-09100IS installation (Jeol) at 7 kV and a 4° angle tilt. After TEM studies, the TEM foil of the alloy irradiated with $E_s = 15$ J cm^{-2} was investigated by electron backscatter diffraction (EBSD) analysis in an Apreo 2 FEGSEM microscope. The scan size was $100 \times 80\,\mu m$, and the step size was 0.5 μm. Furthermore, the surface morphology and roughness of the samples were examined with a noncontact type optical profilometer (Nanofocus-μscan 3-D measurement system).

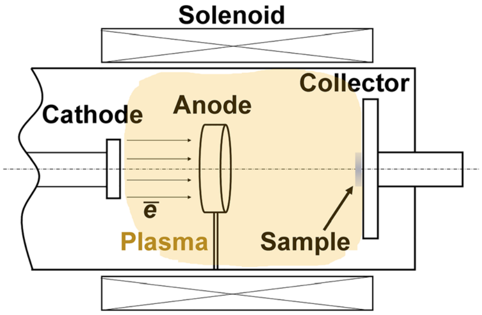

Figure 2. Schematic presentation of the LEHCEB irradiation system.

Nanoindentation tests were performed from the cross-sections of the samples to determine the change in surface hardness of the alloy after the irradiation process. After the microstructural investigations, one energy density was chosen for the nanohardness measurements to see the effect of LEHCEB on the nanohardness behavior of the alloy. Since 15 J cm^{-2} brought about the deepest modified layer, the samples processed using this energy density were used for nanoindentation tests. Load and dwell time were chosen to be 5 mN and 5 s, respectively. Nanoindentation hardness (H_v) values were estimated from the load–displacement (P–h) curves using the Oliver–Pharr method[51]

$$H_v = \frac{P_{\max}}{A_p} \tag{1}$$

where $P_{\max}$ is the maximum indentation load, and A_p is the projected area of indentation. Five different measurements were performed from 2.5 to 3 μm depth of cross-sections of the polished and irradiated samples, and arithmetic means of the hardness values achieved from these measurements were given as the average nanohardness of the samples. The space between each measurement was kept at least 10 μm to avoid being affecting the result of one measurement from the previous ones.

3. Results and Discussion

3.1. Microstructure Analysis

3.1.1. *As-Built Sample*

Figure 3 shows SEM images of the as-built material corresponding to the polished sample in the present study. In general, the microstructure of as-built sample reveals the melt pool boundaries and coarse grains (Figure 3a). Intragranular dendrites also exist in the microstructure (Figure 3b,c). The shape of dendrites varies from extremely elongated (columnar dendrites, outlined with red line in Figure 3b to relatively equiaxed (equiaxed dendrites, outlined with blue line in Figure 3a). The size of equiaxed dendrites ranges from several tenths to several microns. This is a typical microstructure of the Inconel 718 alloy produced by L-PBF AM, as such observations were also reported by some other researchers,[3,4] and related to the strongly directed heat flux during L-PBF.[23,52] In the interdendritic regions, there are irregular-shaped Laves phase (as explained below) with the white contrast in Figure 3a–c formed throughout the material.

Figure 4 shows TEM results obtained from the as-built Inconel-718 alloy. Intragranular columnar dendrites can clearly be seen in Figure 4a. The high-magnification TEM image in Figure 4b shows that the dislocation density is extremely high in the interdendritic regions. As a result, the interdendritic regions look like dark broad lines. Residual stresses due to the high-temperature gradients during the rapid solidification of the as-built material cause microstrains leading to the generation of dislocations. The most of dislocations are in the interdendritic regions, however, dislocation density is also high inside dendrites.[22] TEM images obtained exactly from the same area, but tilted at different angles (Figure 4c,d) indicate that interdendritic regions contain irregular-shaped phases (Figure 4d) besides the high dislocation density (Figure 4c). Precipitate formation in the interdendritic regions can be seen more clearly in the dark field TEM image, as shown in Figure 4e.

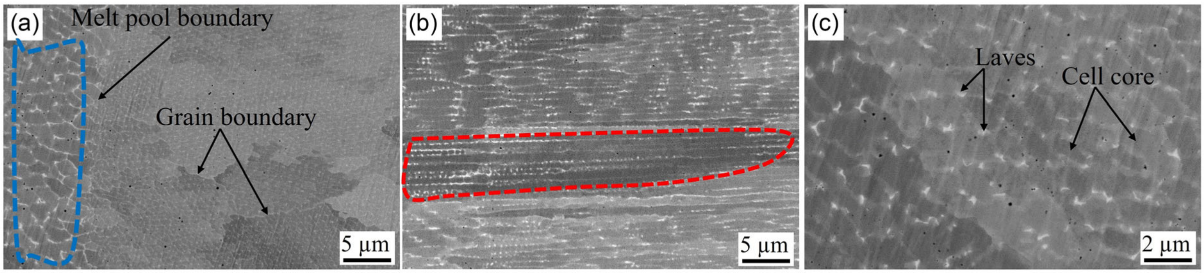

Figure 3. SEM images showing the microstructure of as-built Inconel-718 alloy produced by L-PBF AM. a) Melt pool boundaries, coarse grains, and equiaxed dendrites outlined with blue line, b) elongated dendrites stated with red line, and c) irregular-shaped Laves phase.

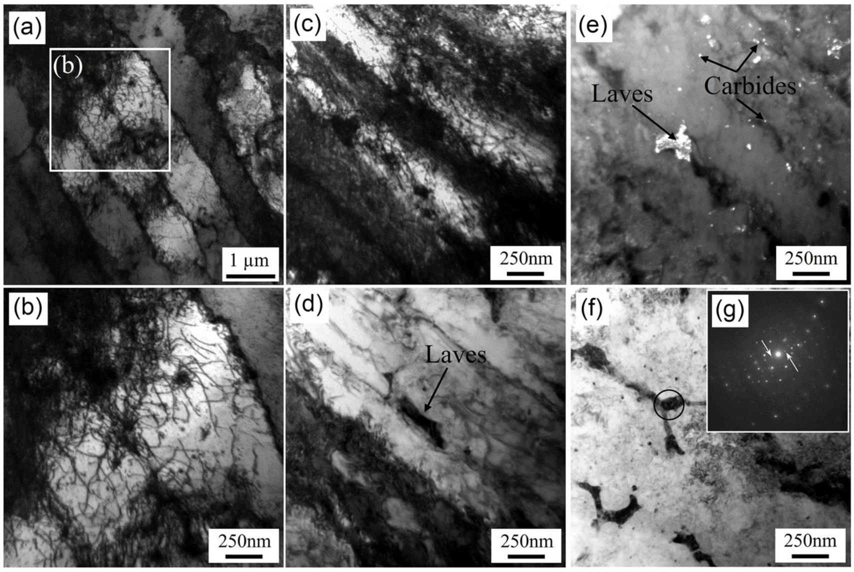

Figure 4. a–f) TEM images showing the microstructure of as-built Inconel 718 alloy. g) SAED pattern taken from the irregularly shaped phase stated with a black circle in (f). a) Intragranular columnar dendrites where the dislocation density is extremely high as seen in (b). c) High dislocation density and d) irregular-shaped phases in the interdendritic regions. e) Precipitate formation in the interdendritic regions. g) SAED pattern showing the Laves phase formation.

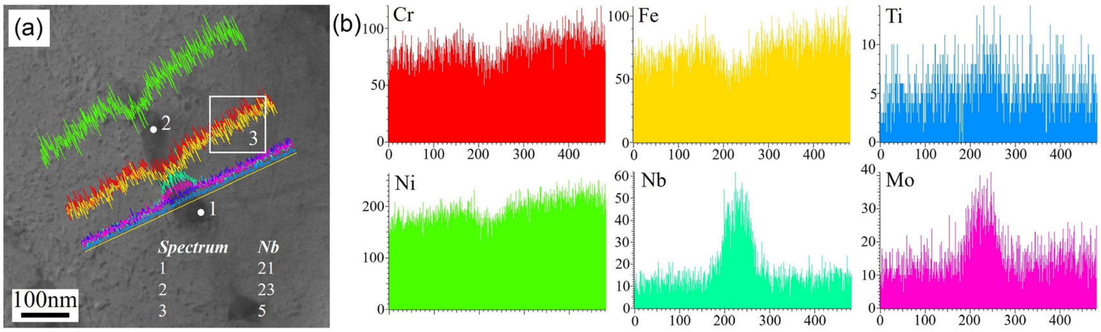

Figure 5. EDX line scanning results: a) the area from where the EDX analyses were performed and b) the distribution of elements along the line. Higher Nb concentration in the particles as compared to the matrix shows the formation of the irregular-shaped Laves phase during L-PBF process.

SAED pattern obtained from the region specified with a circle in Figure 4f shows that two spots closest to the central spot correspond to the Laves phase (Figure 4g). EDX analyses were performed on the irregular shaped phase to determine chemical composition and line scanning results are shown in **Figure 5**. Nb and Mo peaks on the scanned line in Figure 5b confirm that the phase is Laves which is generally considered to be in the form of A_2B, where A corresponds to Ni, Fe, and Cr, while B corresponds to Mo, Nb, and Ti.[53,54] Nb concentration in the irregular-shaped phase and matrix phase (γ) is presented in Figure 5a besides the points and area are analyzed. It is seen that irregular-shaped phase contains ≈21–23 wt% Nb while only ≈5 wt% Nb exists in the matrix γ phase. Considering that Nb concentration in the Laves phase ranges between 10 and 30 wt%,[53] the higher Nb concentration in the particles relative to the matrix provides additional evidence for the formation of the irregular-shaped Laves phase during L-PBF process. The laves phase occurs at the interdendritic region as a result of microsegregation of alloying elements due to rapid solidification of molten pool during the L-PBF process.[4] It is known that Nb, Mo, and Ti are less soluble in Ni as compared to Fe and Cr. Therefore, Fe and Cr are likely to dissolve more in the solid than in the liquid while Nb, Mo, and Ti segregate in the remaining liquid phase during solidification.[52] Consequently, the cores of the cells are the first solidified regions and they are richer in Fe and Cr and poorer in Nb, Mo, and Ti as compared to the interdendritic region as can clearly be seen from the line scanning EDX results in Figure 5a,b. The remaining liquid phase solidifies with two eutectic transformations.[52,55] First, the $L \rightarrow L + \gamma + \text{carbides}$ transformation occurs until all of the carbon in the liquid is used. According to this transformation, it can be concluded that small spherical precipitates at the inter-dendritic and intra-dendritic regions are carbides (NbC) (Figure 4e).[52] At the final stage of the solidification process, $L \rightarrow \gamma + \text{Laves}$ transformation takes place.[53,56] Hence, relatively coarse Laves phases with an irregular shape form at the interdendritic regions, as can be seen in Figure 4d–f.

3.1.2. LEHCEB-Processed Samples

Surface Properties: SEM images representing the surface morphologies of the irradiated samples are given in **Figure 6**. Relatively coarse microcraters of about 100 μm in size are rarely observed on the surface of the sample after LEHCEB irradiation with E_s of 5 J cm^{-2} (Figure 6a, indicated with arrow). There are no coarse microcraters on the surface after irradiation with E_s 10 and 15 J cm^{-2} (Figure 6b,c). It is generally adopted that the microcraters appear around the nonmetallic inclusions in metal materials.[57–60] As Inconel 718 contains no nonmetallic inclusions, the craters appear probably around impurity particles. It may be assumed that the inclusions evaporate or solute in the matrix during the first pulses of LEHCEB irradiation with enhanced E_s, therefore, the coarse craters disappear after the complete series of pulses.

The great number of dislocation slip bands can clearly be seen on the irradiated surface of samples irradiated with all E_s at higher magnification (Figure 6b,d,f). Similar results were also observed in the LEHCEB processed high-speed steel,[61] stainless steel,[62] and Ti-6Al-4V alloy.[63,64] Ozur et al.[65] showed that compressive stresses formed due to the resolidification on the surface of Fe target can reach a few GPa after the irradiation process. Such a high compressive stress value exceeds significantly the yield strength of the Inconel 718 alloy. Thus, it can be concluded that thermal stresses due to the high-temperature gradients during the rapid solidification of the remelted layer resulted in a strong strain of the near-surface layer of the irradiated samples.[61]

Figure 7 shows 3-D profilometric images of the polished and irradiated Inconel 718 sample. The results are well consistent with the surface appearances of the samples illustrated in Figure 6. The surface of the polished sample is quite smooth with R_a of 0.19 ± 0.03 μm (Figure 7a). After irradiation with E_s of 5 J cm^{-2}, the arithmetic surface roughness of the sample was measured as 0.32 ± 0.03 μm, as shown in Figure 7b, indicating the LEHCEB irradiation increases the surface roughness of the sample. Increasing E_s results in higher surface roughness. R_a values of the samples irradiated with E_s of 10 and 15 J cm^{-2} are measured as 0.38 ± 0.04 and 0.44 ± 0.03 μm, respectively.

Cross-Sectional Analysis: **Figure 8** shows the SEM images obtained from a cross-section of the LEHCEB processed samples. In general, the thickness of the remelted layer increases with increasing of E_s (Figure 8a–f). It is measured from the SEM images as 2.3, 3.8, and 5.4 μm for the samples irradiated with E_s of 5, 10, and 15 J cm^{-2}, respectively. SEM images indicate that the LEHCEB irradiation brings about significant microstructural alteration. Intragranular dendrites disappear in the modified

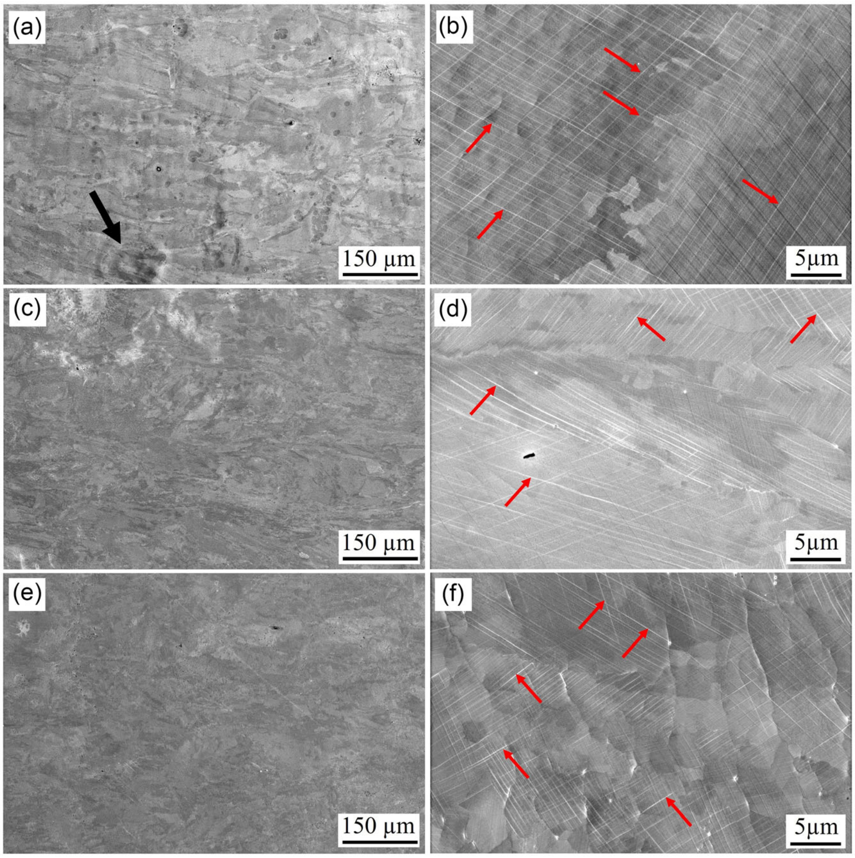

Figure 6. SEM images showing the surface appearances of the polished + irradiated samples; a,b) 5 J cm^{-2}, c,d) 10 J cm^{-2}, and e,f) 15 J cm^{-2}. Dislocation slip bands are indicated with red arrows. The black arrow indicates the coarse crater on the surface in (a).

layer after irradiation with all three E_s (Figure 8a–f). It shows that Laves phases dissolve during the LEHCEB processing of the Inconel 718 alloy.

TEM analysis was performed to examine the microstructural alteration in the modified layer in detail. Some representative TEM images are shown in **Figure 9–11**. Figure 8a–e illustrates the TEM images of the sample irradiated with E_s of 5 J cm^{-2}. One can see from Figure 9a that the modified near-surface layer has a completely different appearance than the as-built region. Dislocations located mostly in interdendritic regions are evident in the as-built region while such a formation is not observed in the modified layer (Figure 9a). Laves phase and carbide particles with bright contrast dissolve in the modified layer, as shown in Figure 9b. This finding is consistent with the data obtained by SEM (Figure 8). The modified layer contains the regions with high dislocation density (Figure 9c) and individual dislocations (Figure 9d). Thin solid stripes parallel to the surface or oriented at an angle of 40 degrees to the horizontal also exist in the modified layer (Figure 9d, indicated with arrows). However, there are no extra spots in the SAED pattern (Figure 9f) taken from the region specified with a circle in Figure 9e. This suggests the lack of Laves and/or carbide phases having different lattice parameters than γ-phase crystal along these solid stripes.

Figure 10 shows TEM images of the sample irradiated with E_s of 10 J cm^{-2}. The equiaxed dendrites seen in the as-built regions do not appear in the modified layer (Figure 10a). Almost all of the modified layer exhibits columnar structure (Figure 10b,c). The width of the columns is ≈130 nm. The boundaries of columns are precipitates of a secondary phase because the neighboring columns show the same crystal orientation and they are undoubtedly the same grain in most cases. This is confirmed by SAED patterns obtained from the areas involving several columns and EBSD maps discussed in the following paragraphs. The SAED pattern taken from the region specified with a circle in Figure 10d reflects no extra spots besides the spots of γ phase, therefore, neither Laves nor carbide phases form at the boundaries of the columns. These phase interlayers forming the columnar boundaries are most likely the same phase as the stripes observed in the modified layer after irradiation with E_s of 5 J cm^{-2}. Evidence of plastic deformation in the modified layer can clearly be observed in the TEM image in Figure 10c.

The representative TEM images of the sample irradiated with E_s of 15 J cm^{-2} are given in Figure 11. Columnar structure exists in the modified layer just in the case of material irradiated with 10 J cm^{-2} (Figure 11a,b). A high-magnification TEM image of the columnar structure shown in Figure 11b helps us to examine this formation. It is apparent that the columns contain high dislocation density and entangled dislocations almost filled the entire column indicating the occurrence of plastic deformation led by thermal stresses due to the high-temperature gradients during

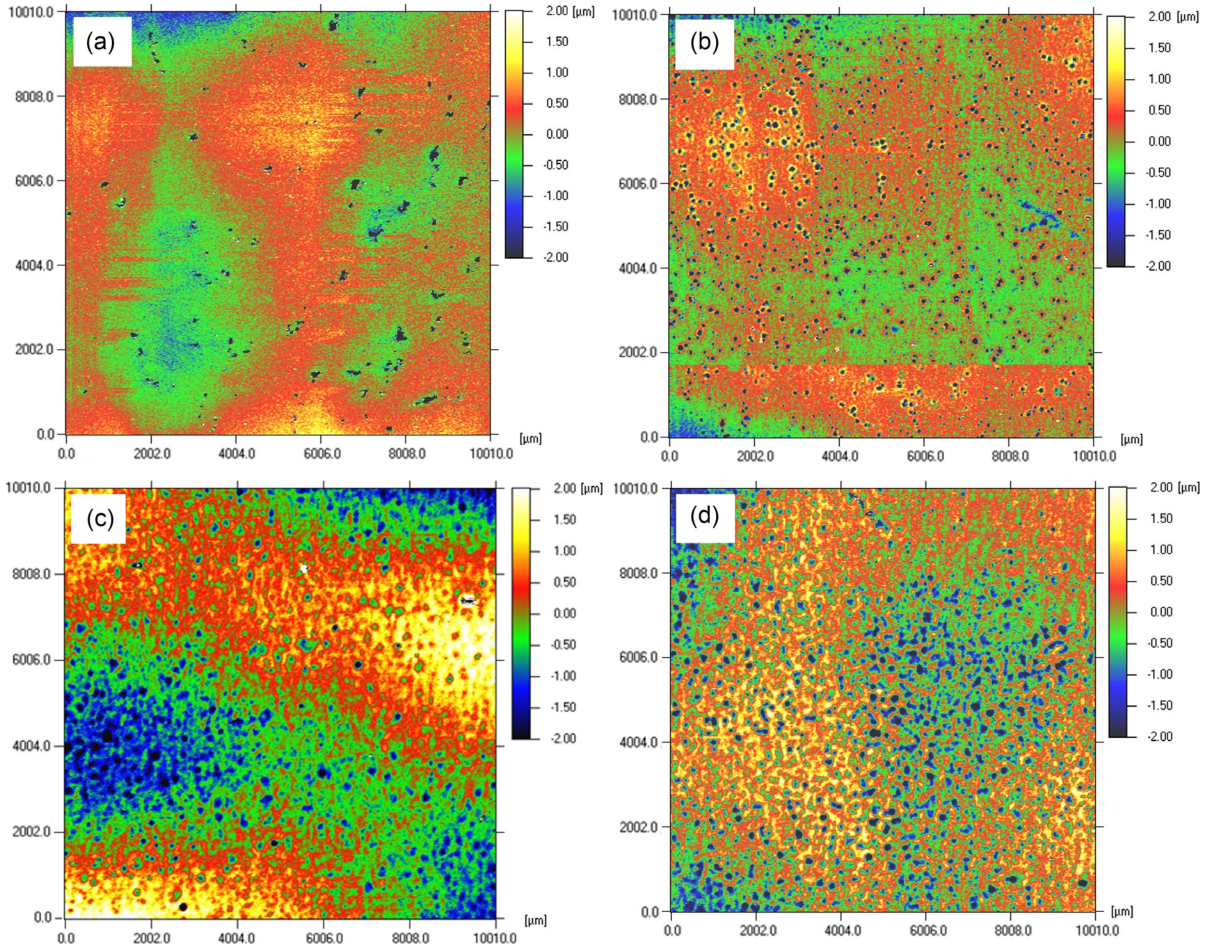

Figure 7. 3-D profilometer images of Inconel 718 alloy for the polished and irradiated conditions: a) polished sample and b–d) irradiated samples of b) 5 J cm^{-2}, c) 10 J cm^{-2}, and d) 15 J cm^{-2}.

the rapid solidification of the remelted layer. The appearance of residual stresses in the near-surface layer is the characteristic feature of materials processed with LEHCEB.[66–68] Moreover, the dislocation slip bands observed on the surface of the samples (Figure 6) suggest the occurrence of plastic deformation during LEHCEB irradiation.

It should be noted that the width of columns is significantly lower than that of columnar dendrites observed in the as-built sample. Therefore, it can be concluded that the columns are newly formed structures that appeared during LEHCEB processing of the Inconel 718 alloy. It is believed that the stripes and columnar boundaries existing in the structure of the modified layer after irradiation with E_s of 5 and 10 J cm^{-2}, respectively, have the same nature. TEM image obtained from just near the modified layer confirms that columnar structure does not exist in the as-built region (Figure 11c). The dark field TEM image given in Figure 11d shows that the visible boundaries of columns are decorated with very thin interlayers of precipitates formed during the LEHCEB irradiation. There are no extra reflexes in the SAED pattern taken from the area circled in Figure 11e. However, when the foil is tilted in the TEM column, these very thin interlayers are highlighted together with columns in the dark field image obtained from the nearest reflection to the central one in Figure 11f (the highlighted interlayer is indicated with yellow arrows in Figure 11d). This indicates the phase forming the interlayers shows the same (or at least very close) parameters as γ phase parameters.

Laves phases have higher interplane distance than γ phase, therefore, they must give the respective reflections in SAED patterns. The absence of the reflections definitely indicates that precipitates are not Laves phases. The other candidates for this phase are γ' and γ'' but they also have some interplane distances different from those in γ phase. Moreover, the precipitation of the latter two phases is not possible theoretically during the rapid solidification of the modified layer after LEHCEB irradiation.[52] Indeed, small particles of γ'' phases were observed in the as-built structure of the Inconel 718 alloy produced via L-PBF[52,69] when a cooling rate of 10^5–10^7 K s^{-1},[1,70] which is lower than that under LEHCEB pulse action ($\approx 10^9$ K s^{-1}[36]). The three-order of magnitude difference in the cooling rate inhibits the precipitation of γ' and γ'' strengthening phases. Furthermore, it was stated that γ'' phase particles were precipitated due to the thermal cycle during the following laser scans.[52,69] Such a thermal cycle, in contrast, does not exist on the modified layer of

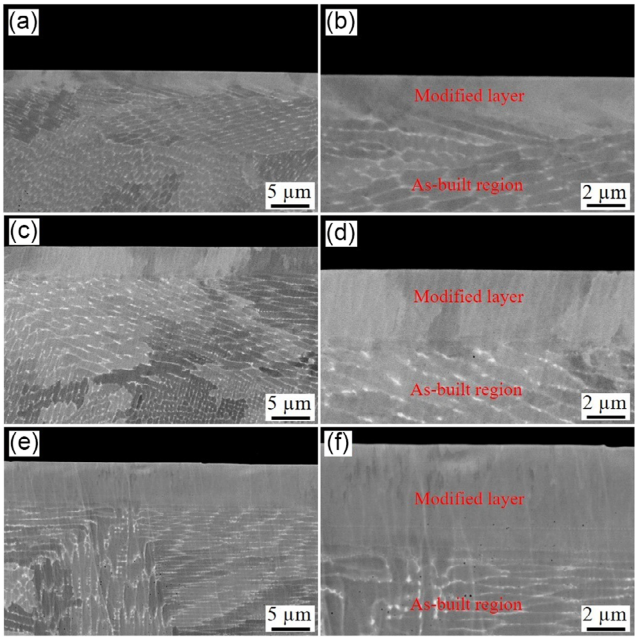

Figure 8. SEM images in cross-section of the samples which are LEHCEB processed with E_s of: a,b) 5 J cm^{-2}, c,d) 10 J cm^{-2}, and e,f) 15 J cm^{-2}. Intragranular dendrites disappear in the modified layer after irradiation with all three E_s.

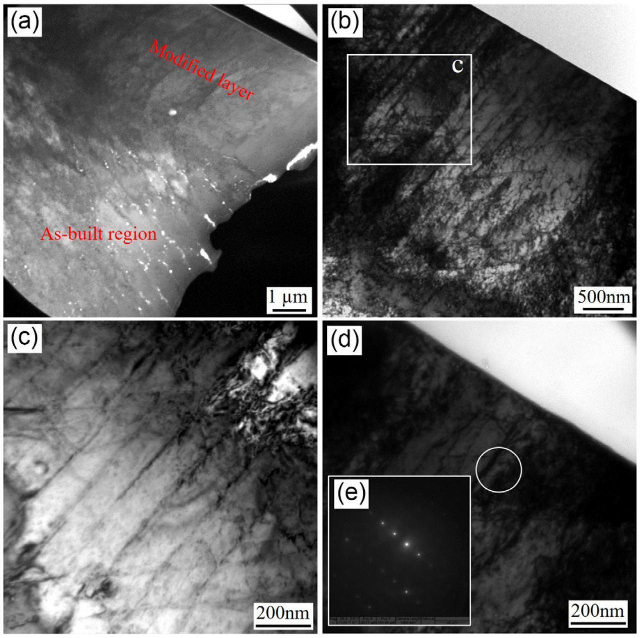

Figure 10. a–d) TEM images showing the microstructure of the modified layer of the sample irradiated with E_s of 10 J cm^{-2}. e) The SAED pattern obtained from the region is indicated with a white circle in (d). The sign of plastic deformation in the modified layer can be seen in (c).

LEHCEB-irradiated Inconel 718 alloy. Thus, the nature of the precipitations phase requires additional investigations.

There is high dislocation density in the modified layer between the interlayers of precipitates. These interlayers inhibit the movement of dislocation during plastic deformation induced by thermal stresses. Therefore, the areas between the columns look like grain or subgrain boundaries due to the precipitates and high dislocation density. But actually, they are neither subgrain nor grain boundaries.

Microstructural alteration on the modified layer of the LEHCEB irradiated samples was further analyzed with EBSD and some representative images of the sample irradiated with

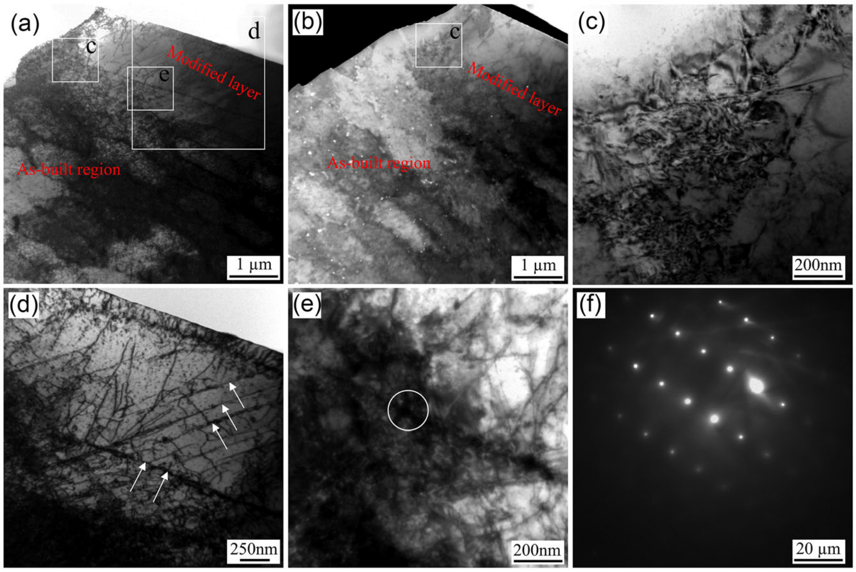

Figure 9. a–e) TEM images showing the microstructure of the modified layer of the sample irradiated with E_s of 5 J cm^{-2}. f) The SAED pattern is taken from the region indicated with a white circle in (e). The modified layer does not contain Laves phase and carbide particles (b). The regions containing (c) high dislocation density and (d) individual dislocations in the modified layer. White arrows show thin solid stripes (d). No extra spots in the SAED pattern in (f) indicate the lack of Laves and/or carbide phases at the solid stripes.

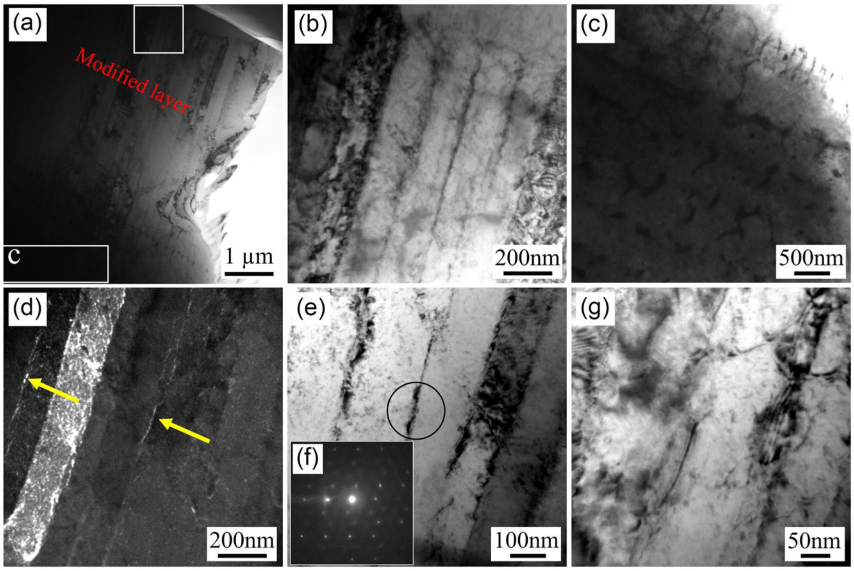

Figure 11. a–e,g) TEM images showing the microstructure of the modified layer of the sample irradiated with E_s of 15 J cm^{-2}. f) SAED pattern taken from the region indicated with a black circle in (e). b) The columns contain high dislocation density and entangled dislocations. d) The visible boundaries of columns are decorated with very thin interlayers of precipitates. f) SAED pattern taken indicates the phase forming the interlayers shows the same (or at least very close) parameters as γ phase parameters.

E_s of 15 J cm^{-2} are given in **Figure 12**. Inverse pole figure map in Figure 12a and grain boundaries map in Figure 12b show that the modified layer contains coarse grains just in the case of the as-built sample and no any grain refinement occurs during the irradiation process. This observation provides another evidence that the columns in the apparent columnar structure in the modified layer are not separated from each other by grain or subgrain boundaries. The areas between the columns look like subgrain boundaries due to the precipitates and high dislocation density.[14]

3.2. Nanohardness Behavior

Typical P–h curves obtained from the nanoindentation tests are shown in **Figure 13**. As clearly seen, the sample irradiated with E_s of 15 J cm^{-2} exhibits relatively lower displacement than the polished one which indicates a higher nanoindentation hardness value. From the nanoindentation tests, hardness values were calculated as 593 ± 23 and 693 ± 13 H_v for the polished and polished + irradiated samples, respectively. It should be noted that the H_v values given here are different from the H_v obtained from the Vickers microhardness for two reasons. First, A_p is the projected area of indentation in Equation (1) while it is taken as the surface area for conventional Vickers hardness.[71] Indentation size also affects the achieved hardness, and decreasing indentation load P results in an increase in H for sharp indentations.[72–74] It is seen that the surface nanohardness of the Inconel 718 alloy is increased by 17% after the irradiation process. Such an increment in the nanoindentation hardness (H_v) can be attributed mainly to the formation of a columnar

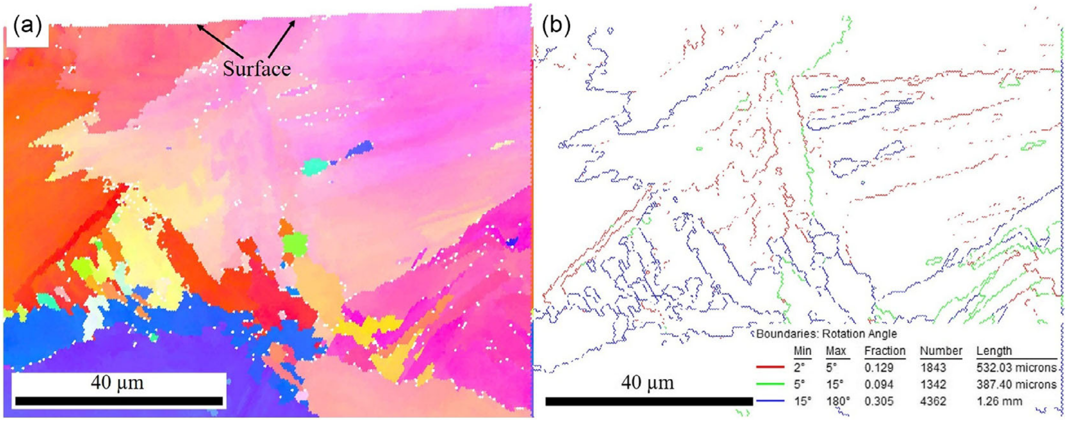

	Min	Max	Fraction	Number	Length
🟥	2°	5°	0.129	1843	532.03 microns
🟩	5°	15°	0.094	1342	387.40 microns
🟦	15°	180°	0.305	4362	1.26 mm

Figure 12. a) Inverse pole figure map and b) grain boundaries map of the near-surface area of the sample irradiated with E_s of 15 J cm^{-2}. The modified layer contains coarse grains just in the case of the as-built sample.

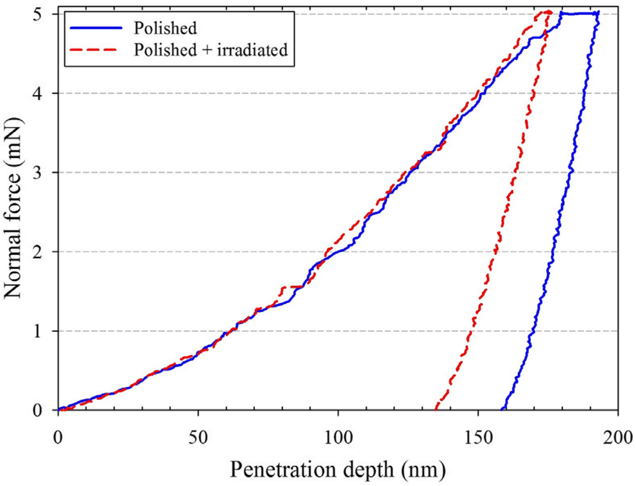

Figure 13. Load–displacement curves for the polished (corresponds to the as-built sample) and polished + irradiated (15 J cm^{-2}) samples.

structure where the columns are separated from each other by the district regions containing high amount of dislocations. The dendrite structure in the as-built sample also has a positive impact on the hardness of the sample.[75] However, the width of columns in the modified layer of the irradiated sample is much smaller than the spaces between the interdendritic regions of the as-built sample. Thus, the hardening effect of the columnar structure of the irradiated sample is more pronounced as compared to the interdendritic regions of the as-built sample. It is a well-known fact that phase composition also has a substantial effect on the hardness of the Inconel 718 alloy. Almost all of the Laves phase which is known to be detrimental to the material strength dissolved during the irradiation process (Figure 8–11). It was stated that a high amount of Laves weakens the γ phase since it consumes large amounts of niobium and also limits the formation of strengthening phases.[2,20] Therefore, the dissolution of Laves phase may be considered as another reason for the increment in hardness after the irradiation process.

4. Conclusion

In this study, the effect of LEHCEB on the microstructure and nanohardness of Inconel 718 alloy produced by L-PBF AM was investigated. The following can be concluded from the present study: 1) The microstructure of the as-built alloy mostly consists of intragranular dendrites. Interdendritic regions contain enhanced dislocation density and irregular-shaped phases. EDX analyses showed that irregular shaped phases are Laves containing high (in the ranges between 10 and 30 wt%) amounts of Nb. Besides, small spherical carbides (NbC) also exist in the as-built microstructure; 2) LEHCEB irradiation of Inconel 718 alloy produced by L-PBF brings about significant microstructural alteration. Columnar structure with the columns having a much lower width than the most elongated dendrites of the as-built sample covers almost all of the modified layer. Precipitations of a secondary phase together with adjacent dislocations form the boundaries of columns. High dislocation density and entangled dislocations appear as a result of plastic deformation led by thermal stresses due to the high-temperature gradients during the rapid solidification of the remelted layer; 3) All of Laves phases dissolved in the modified layer of the samples irradiated with energy densities from 5 to 15 J cm^{-2}; and 4) Surface nanoindentation hardness of the alloy increased from $593 \pm 23\ H_v$ for the polished as-build sample to $693 \pm 13\ H_v$ for the sample after irradiation with the highest energy density of 15 J cm^{-2}. Such an increment in the nanoindentation hardness H_v is attributed to the formation of ultrafine columnar structure with the columns separated from each other by the district regions containing secondary phase precipitations and a high number of dislocations in the vicinity of precipitations. The dissolution of Laves phase is considered another reason for the increment in hardness after the irradiation.

Acknowledgements

A part of this work was performed according to the Russian Government research assignment for ISPMS SB RAS (project FWRW-2021-0003). Access to the experimental equipment in the “Nanotech” Common Use Center (ISPMS SB RAS) is acknowledged.

Conflict of Interest

The authors declare no conflict of interest.

Data Availability Statement

The data that support the findings of this study are available from the corresponding author upon reasonable request.

Keywords

additive manufacturing, Inconel-718, irradiation, low-energy high-current electron beam, microstructure, nanohardness, phase composition

Received: March 12, 2024
Revised: May 16, 2024

---

[1] X. Li, J. J. Shi, C. H. Wang, G. H. Cao, A. M. Russell, Z. J. Zhou, C. P. Li, G. F. Chen, *J. Alloys Compd.* **2018**, *764*, 639.
[2] A. Tajyar, N. Brooks, N. Holtham, R. Rowe, D. J. Newell, A. N. Palazotto, K. Davami, *Mater. Sci. Eng. A* **2022**, *838*, 142770.
[3] S. Luo, W. Huang, H. Yang, J. Yang, Z. Wang, X. Zeng, *Addit. Manuf.* **2019**, *30*, 100875.
[4] E. Chlebus, K. Gruber, B. Kuźnicka, J. Kurzac, T. Kurzynowski, *Mater. Sci. Eng. A* **2015**, *639*, 647.
[5] A. Devillez, F. Schneider, S. Dominiak, D. Dudzinski, D. Larrouquere, *Wear* **2007**, *262*, 931.
[6] H. Lu, X. Jia, K. Zhang, C. Yao, *Mater. Sci. Eng. A* **2002**, *326*, 382.
[7] S. M. Gaytan, L. E. Murr, F. Medina, E. Martinez, M. I. Lopez, R. B. Wicker, *Mater. Technol.* **2009**, *24*, 180.
[8] H. L. Wei, J. S. Zuback, T. Mukherjee, J. W. Elmer, J. O. Milewski, A. M. Beese, A. Wilson-Heid, A. Ded, *Prog. Mater. Sci.* **2018**, *92*, 112.
[9] D. Herzog, V. Seyda, E. Wycisk, C. Emmelmann, *Acta Mater.* **2016**, *117*, 371.

[10] G. Li, W. Chi, W. Wang, X. Liu, H. Tu, X. Long, *Fatigue* **2024**, *184*, 108287.
[11] A. K. Syed, W. Vesga, B. Dutton, T. Berentshaw, X. Zhang, *Fatigue* **2024**, *184*, 108285.
[12] T. D. Piette, A. G. Spangenberger, B. E. Stoner, D. A. Lados, *J. Manuf. Process.* **2024**, *118*, 419.
[13] Y. Karabulut, E. Tascioglu, Y. Kaynak, *Optik* **2021**, *227*, 163907.
[14] W. M. Tucho, P. Cuvillier, A. Sjolyst-Kverneland, V. Hansen, *Mater. Sci. Eng. A* **2017**, *689*, 220.
[15] N. Kouraytem, J. Varga, B. Amin-Ahmadi, H. Mirmohammad, R. A. Chanut, A. D. Spear, O. T. Kingstedt, *Mater. Des.* **2021**, *198*, 109228.
[16] Y.-J. Kang, S. Yang, Y.-K. Kim, B. AlMangour, K.-A. Lee, *Corros. Sci.* **2019**, *158*, 108082.
[17] ASTM B670-07, *Standard Specification for Precipitation-Hardening Nickel Alloy (UNS N07718) Plate, Sheet, and Strip for High-Temperature Service 1*. ASTM, West Conshohocken, PA **2018**.
[18] S. Sui, H. Tan, J. Chen, C. Zhong, Z. Li, W. Fan, A. Gasser, W. Huang, *Acta Mater.* **2019**, *164*, 413.
[19] D. Zhang, W. Niu, X. Cao, Z. Liu, *Mater. Sci. Eng. A* **2015**, *644*, 32.
[20] Y. Zhang, Z. Li, P. Nie, Y. Wu, *Metall. Mater. Trans. A* **2013** *44*, 708.
[21] J. Strößner, M. Terock, U. Glatzel, *Adv. Eng. Mater.* **2015**, *17*, 1099.
[22] T. G. Gallmeyer, S. Moorthy, B. B. Kappes, M. J. Mills, B. Amin-Ahmadi, A. P. Stebner, *Addit. Manuf.* **2020**, *31*, 100977.
[23] M. Aydinöz, F. Brenne, M. Schaper, C. Schaak, W. Tillmann, J. Nellesen, T. Niendorf, *Mater. Sci. Eng. A* **2016**, *669*, 246.
[24] M. Pröbstle, S. Neumeier, J. Hopfenmüller, L. Freund, T. Niendorf, D. Schwarze, M. Göken, *Mater. Sci. Eng. A* **2016**, *674*, 299.
[25] K. Moussaoui, W. Rubio, M. Mousseigne, T. Sultan, F. Rezai, *Mater. Sci. Eng. A* **2018**, *735*, 182.
[26] K. N. Amato, S. M. Gaytan, L. E. Murr, E. Martinez, P. W. Shindo, J. Hernandez, S. Collins, F. Medina, *Acta Mater.* **2012**, *60*, 2229.
[27] B. B. Babamiri, J. Indeck, G. Demeneghi, J. Cuadra, K. Hazeli, *Addit. Manuf.* **2020**, *34*, 101380.
[28] W. Tillmann, C. Schaak, J. Nellesen, M. Schaper, M. E. Aydinoz, K. P. Hoyer, *Addit. Manuf.* **2017**, *13*, 93.
[29] P. L. Blackwell, *J. Mater. Process. Technol.* **2005**, *170*, 240.
[30] D. A. Lesyk, S. Martinez, B. N. Mordyuk, V. V. Dzhemelinskyi, A. Lamikiz, G. I. Prokopenko, *Surf. Coat. Technol.* **2020**, *381*, 125136.
[31] C. Yu, Z. Huang, Z. Zhang, J. Wang, J. Shen, Z. Xu, *J. Mater. Res. Technol.* **2022**, *18*, 29.
[32] A. N. Jinoop, S. Kanmani Subbu, C. P. Paul, I. A. Palani, *Int. J. Precis. Eng. Manuf.* **2019**, *20*, 1621.
[33] V. N. Devyatkov, Yu. F. Ivanov, O. V. Krysina, N. N. Koval, E. A. Petrikova, V. V. Shugurov, *Vacuum* **2017**, *143*, 464.
[34] V. Engelko, B. Yatsenko, G. Mueller, H. Bluhm, *Vacuum* **2001**, *62*, 211.
[35] D. I. Proskurovsky, V. P. Rotshtein, G. E. Ozur, *Surf. Coat. Technol.* **2000**, *125*, 49.
[36] D. I. Proskurovsky, V. P. Rotshtein, G. E. Ozur, A. B. Markov, D. S. Nazarov, V. A. Shulov, *J. Vac. Sci. Technol. A* **1998**, *16*, 2480.
[37] G. E. Ozur, D. I. Proskurovsky, *Phys. Rep.* **2018**, *44*, 18.
[38] X. D. Zhang, S. Z. Hao, X. N. Li, C. Dong, T. Grosdidier, *Appl. Surf. Sci.* **2011**, *257*, 5899.
[39] S. Hao, S. Yao, J. Guan, A. Wu, P. Zhong, C. Dong, *Curr. Appl. Phys.* **2001**, *1*, 203.
[40] K. Zhang, J. Zou, T. Grosdidier, *J. Vac. Sci. Technol. A* **2010**, *28*, 1349.
[41] S. Hao, H. Wang, L. Zhao, *Nucl. Instrum. Methods Phys. Res. B* **2016**, *368*, 81.
[42] Y. Hao, B. Gao, G. F. Tu, H. Cao, S. Z. Hao, C. Dong, *Appl. Surf. Sci.* **2012**, *258*, 2052.
[43] Y.-K. Gao, *J. Alloys Compd.* **2013**, *572*, 180.
[44] G. Guo, G. Tang, X. Ma, M. Sun, G. E. Ozur, *Surf. Coat. Technol.* **2013**, *229*, 140.
[45] Z. M. Zhou, L. Chai, Z. Xiao, J. Tu, Y. P. Wang, W. J. Huang, *Trans. Nonferrous Met. Soc. China* **2015**, *25*, 1935.
[46] L. J. Chai, Z. M. Zhou, Z. P. Xiao, J. Tu, Y. P. Wang, W. J. Huang, *Sci. China. Technol. Sci.* **2015**, *58*, 462.
[47] M. Demirtas, K. V. Ivanov, G. Purcek, H. Yanar, *J. Alloys Compd.* **2022**, *898*, 162860.
[48] K. V. Ivanov, A. E. Chesnokov, A. V. Smirnov, *Vacuum* **2022**, *197*, 110780.
[49] T. Shinonaga, H. Kobayashi, A. Okada, T. Tsuji, *Int. J. Adv. Manuf. Technol.* **2023**, *127*, 5127.
[50] P. P. Kiziridi, G. E. Ozur, *Tech. Phys.* **2015**, *60*, 917.
[51] W. C. Oliver, G. M. Pharr, *J. Mater. Res.* **1992**, *7*, 1564.
[52] M. Calandri, D. Manfredi, F. Calignano, E. Paola Ambrosio, S. Biamino, R. Lupoi, D. Ugues, *Adv. Eng. Mater.* **2018**, *20*, 1800351.
[53] C. Radhakrishna, K. P. Rao, *J. Mater. Sci.* **1997**, *32*, 1977.
[54] J. J. Schirra, R. H. Caless, R. W. Hatala, in *Superalloys 718, 625 and Various Derivatives* (Ed: E. A. Loria), TMS, Pittsburgh, PA **1991**.
[55] G. A. Knorovsky, M. J. Cieslak, T. J. Headley, A. D. Romig Jr., W. F. Hammetter, *Metall. Trans. A* **1989**, *20*, 2149.
[56] S. G. K. Manikandan, D. Sivakumar, K. Prasad Rao, M. Kamaraj, *Mater. Charact.* **2015**, *100*, 192.
[57] G. E. Ozur, D. I. Proskurovsky, V. P. Rotshtein, *Phys. Lett.* **2016**, *42*, 328.
[58] J. Zou, K. Zhang, C. Dong, Y. Qin, *Appl. Phys. Lett.* **2006**, *89*, 041913.
[59] Y. Qin, C. Dong, X. Wang, *J. Vac. Sci. Technol. A* **2003**, *21*, 1934.
[60] K. Zhang, J. Zou, T. Grosdidier, C. Dong, D. Yang, *Surf. Coat. Technol.* **2006**, *201*, 1393.
[61] Y. Ivanov, W. Matz, V. Rotshtein, R. Günzel, N. Shevchenko, *Surf. Coat. Technol.* **2002**, *150*, 188.
[62] K. V. Ivanov, K. O. Akimov, M. Demirtas, G. Purcek, *Vacuum* **2024**, *225*, 113205.
[63] J. C. Walker, J. W. Murray, M. Nie, R. B. Cook, A. T. Clare, *Appl. Surf. Sci.* **2014**, *311*, 534.
[64] V. P. Rotshtein, V. A. Shulov, *J. Metall.* **2011**, *2011*, 673685.
[65] G. E. Ozur, D. I. Proskurovsky, V. P. Rotshtein, A. B. Markov, *Laser Particle Beams* **2003**, *21*, 157.
[66] E. F. Dudarev, G. P. Pochivalova, D. I. Proskurovskii, V. P. Rotshtein, A. B. Markov, *Russ. Phys. J.* **1996**, *39*, 284.
[67] W. Jiang, Y. Sun, H. Dai, E. Wang, *Nucl. Instrum. Methods Phys. Res. B* **2023**, *542*, 7.
[68] L. L. Meisner, V. O. Semin, Yu. P. Mironov, S. N. Meisner, F. A. D'yachenko, *Mater. Today Commun.* **2018**, *17*, 169.
[69] Y. Tian, D. McAllister, H. Colijn, M. Mills, D. Farson, M. Nordin, S. Babu, *Metall. Mater. Trans. A* **2014**, *45*, 4470.
[70] J.-P. Choi, G.-H. Shin, S. Yang, D.-Y. Yang, J.-S. Lee, M. Brochu, J.-H. Yu, *Powder Technol.* **2017**, *310*, 60.
[71] N. Q. Chinh, R. Z. Valiev, X. Sauvage, G. Varga, K. Havancsak, M. Kawasaki, B. B. Straumal, T. G. Langdon, *Adv. Eng. Mater.* **2014**, *16*, 1000.
[72] W. D. Nix, H. Gao, *J. Mech. Phys. Solids* **1998**, *46*, 411.
[73] D. Kiener, K. Durst, M. Rester, A. M. Minor, *JOM* **2009**, *61*, 14.
[74] G. M. Pharr, E. G. Herbert, Y. Gao, *Mater. Res.* **2010**, *40*, 271.
[75] S. Holland, X. Wang, J. Chen, W. Cai, F. Yan, L. Li, *J. Alloys Compd.* **2019**, *784*, 182.